GENERATION OF TYPE III SOLAR RADIO BURSTS IN THE LOW CORONA BY DIRECT AMPLIFICATION. II. FURTHER NUMERICAL STUDY

PETER H. YOON,[1] C. S. WU,[1,2] AND C. B. WANG[2]

ABSTRACT

In a recent paper a cyclotron maser model was proposed as an alternative explanation of coronal type III solar radio bursts. However, the discussion was preliminary in that it was limited to a local theory and in that the propagation of the emitted waves was studied with a simplified scheme. The present article complements the earlier study by simultaneously computing the ray trajectory with a more sophisticated approach and estimating the intensity of the amplified waves. Numerical results lead to the conclusion that the $O1$-mode is insignificant despite the robust initial growth rate predicted by local theory, while $X1$- and $X2$-modes are equally important. This finding is consistent with observations and confirms the scenario originally put forward in the earlier paper.

Subject headings: methods: numerical — Sun: corona — Sun: radio radiation

1. INTRODUCTION

In a preceding article (Wu et al. 2002), an alternative scenario for the solar type III radio emission is proposed. The model differs from the standard theories in that instead of the plasma emission process (see the references in Wu et al. 2002), it emphasizes the cyclotron maser process, in which the radiation is produced by a direct linear maser instability mechanism rather than through an indirect nonlinear conversion process. The key underlying assumptions in this model are the presence of flare-associated streaming electrons that possess a distribution with a perpendicular population inversion and the existence of density-depleted flux tubes in the low corona, in which the physical conditions are favorable for the operation of the cyclotron maser instability.

The discussion presented in Wu et al. (2002) is preliminary. It is limited to the local linear growth rate computation such that the saturated wave amplitude could not be estimated. The purpose of this article is to complement the previous work in this regard.

For an inhomogeneous medium, wave saturation may take place as a result of the combined nonlinear and convective processes. For the sake of simplicity, however, we ignore the former process in the present study. When an electromagnetic ray propagates in a plasma with inhomogeneous density and magnetic field, the local wave-particle resonance condition changes spontaneously from place to place. Such a detuning effect leads to the convective saturation of the ray.

To carry out the present study we adopt a scheme that is more sophisticated than that used by Wu et al. (2002). In the present discussion, we solve the equations for ray trajectory while computing local growth rate and wave amplitude concomitantly at each point along the ray path. As a consequence, we are able to address a number of outstanding theoretical issues that must be resolved if the model proposed by Wu et al. (2002) is to be substantiated.

In the following, two relevant issues are described: According to Wu et al. (2002), it is found that for sources located in the low-altitude ranges, the extraordinary mode with a frequency near the fundamental electron gyrofrequency ($X1$) can have spatial (temporal) growth rates that are much higher (lower) than that of the X-mode with a frequency near the harmonic of the gyrofrequency ($X2$). This finding may be interpreted as implying that the intensity of the $X1$-mode should be much higher than that of the $X2$-mode if the amplification is primarily governed by convective growth (if the wave amplification is by temporal growth, then the $X1$-mode should have much lower intensity than the $X2$ mode).

Another issue is that for the source region characterized by $0.4 < f_{pe}/f_{ce} < 1$ (where f_{pe} is the plasma frequency and f_{ce} is the electron gyrofrequency), the $O1$-mode (ordinary mode near the fundamental gyrofrequency) and the $X2$-mode have comparable local growth rates. This result may be interpreted as indicating that the observed fundamental (F) and harmonic (H) components should be characterized by an opposite sense of polarization. However, according to the report by Dulk & Suzuki (1980), in almost all of the F-H pairs observed, the two components have the same sense of polarization (observations cannot distinguish between X- and O-mode polarization—all they can tell is that both the F and H components have the same sense of polarization). Again, the discussion by Wu et al. (2002) could not resolve this issue.

As will be discussed, the present analysis is able to resolve these issues. We will demonstrate, by means of numerical solutions of combined ray tracing/intensity equations, that the $X1$- and $X2$-modes achieve comparable saturation amplitudes and that the convective growth of the $O1$-mode does not rise to a significant level. The organization of the present paper is that § 2 presents the discussion of the physical models, fundamental equations, and numerical results, while § 3 presents the conclusions.

2. MODELING AND NUMERICAL STUDY

2.1. *Magnetic Field Model*

In the present discussion we are concerned with the solar corona in the vicinity of a sunspot. It is very difficult to

[1] Institute for Physical Science and Technology, University of Maryland, College Park, MD 20742.

[2] Department of Earth and Space Sciences, University of Science and Technology of China, Hefei, Anhui 230026, China.

model the sunspot magnetic field in full generality, but for the sake of discussion, we model a unipolar magnetic field along the axis of the sunspot, following Zheleznyakov (1970):

$$B_r = B_0 \left(1 - \frac{h}{\sqrt{h^2 + b^2}}\right) , \quad h = r - R_\odot , \qquad (1)$$

where B_0 (in gauss) is the magnetic field intensity at the base of a sunspot of radius b, and r is the distance measured from the center of the Sun (r and b are given in kilometers), $r = 0$ being the center of the Sun, and $r = R_\odot = 7 \times 10^5$ km being a solar radius. A schematic diagram showing the geometry under consideration is displayed in Figure 1, where θ_P represents the polar angle defined with respect to the axis with the footpoint at the center of the sunspot. To model the entire three-dimensional unipolar magnetic field, we make use of the relation $\nabla \cdot \boldsymbol{B} = 0$,

$$\frac{1}{r^2}\frac{\partial r^2 B_r}{\partial r} + \frac{1}{r \sin \theta_P}\frac{\partial}{\partial \theta_P}(B_{\theta_P} \sin \theta_P) = 0 . \qquad (2)$$

We expect that the angular component of the magnetic field, B_{θ_P}, should vanish when $\theta_P = 0$ and that it should be an odd function of θ_P. On the other hand, the radial magnetic field component, B_r, should be an even function of θ_P and should maximize at $\theta_P = 0$. Armed with this information, it is reasonable to assume that

$$B_r(r, \theta_P) \approx \bar{B}_r(r) \cos \theta_P , \quad B_{\theta_P}(r, \theta_P) \approx \bar{B}_{\theta_P}(r) \sin \theta_P . \quad (3)$$

Inserting equation (3) into equation (2), we obtain the three-dimensional magnetic field (with azimuthal symmetry) valid in the vicinity of the sunspot,

$$\boldsymbol{B}(r, \theta_P) = \hat{r}B_r(r, \theta_P) + \hat{\theta}_P B_{\theta_P}(r, \theta_P) ,$$

$$B_r(r, \theta_P) = B_0 \cos \theta_P \left(1 - \frac{h}{\sqrt{h^2 + b^2}}\right) ,$$

$$B_{\theta_P}(r, \theta_P) = B_0 \sin \theta_P \left[\frac{rb^2/2}{(h^2 + b^2)^{3/2}} - 1 + \frac{h}{\sqrt{h^2 + b^2}}\right] , \quad (4)$$

where $h = r - R_\odot$ is as defined previously.

For the specific choice of physical parameters, we model the reference field strength at the base of the sunspot as $B_0 = 10^3$ G, and choose the sunspot radius as $b = 3.20 \times 10^4$ km (note that $b/R_\odot = 0.0452$). For future reference, the local electron gyrofrequency is given by

$$f_{ce}(r, \theta_P) = 2.80 B(r, \theta_P) \text{ MHz} , \qquad (5)$$

where $B(r, \theta_P) = [B_r^2(r, \theta_P) + B_{\theta_P}^2(r, \theta_P)]^{1/2}$ is the total strength of the local magnetic field. Note that the angular electron gyrofrequency is alternatively given by $\Omega_{ce}(r, \theta_P) = 2\pi f_{ce}(r, \theta_P) = 1.76 \times 10^7 B(r, \theta_P) \text{ rad s}^{-1}$.

Figure 2 shows the plot of the model magnetic field lines computed on the basis of the present model described in equation (4). The distances are all normalized with respect to the solar radius. Figure 2 also shows, in gray scale, the background electron density profile as well as the density-depleted tube that runs vertically at the center, indicated by the dark shaded vertical structure. The modeling of the background electron density and the density-depleted duct will be discussed next.
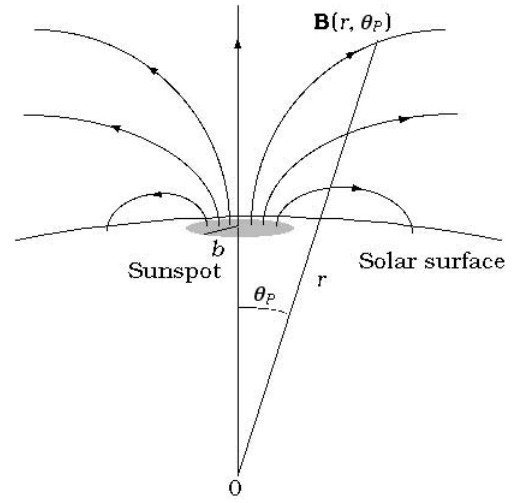

FIG. 1.—Unipolar magnetic field model of a sunspot

2.2. Models of Interior and Exterior Density

In the present scenario, radio emission occurs inside the density duct. We are concerned with a situation in which the streams of energetic electrons are generated near the foot of the sunspot and, which subsequently travel outward along the magnetic field lines. We may envisage a situation in which the source region of the radiation (i.e., the physical location of the electron beam) coincides with a narrow radial tube or density cavity (or duct), with the typical radius of the tube being much smaller than the sunspot radius (see Fig. 2). For the present purpose, the average (background) electron density in the corona will be modeled according to a formula that is qualitatively similar to the Newkirk model (Newkirk 1967),

$$n_e^O(r) = 10^9 (r/R_\odot)^{-6} . \qquad (6)$$

In the above, the superscript "O" is meant to designate the density "outside" the density cavity. We desire to model the density depletion that gradually disappears as the alti-
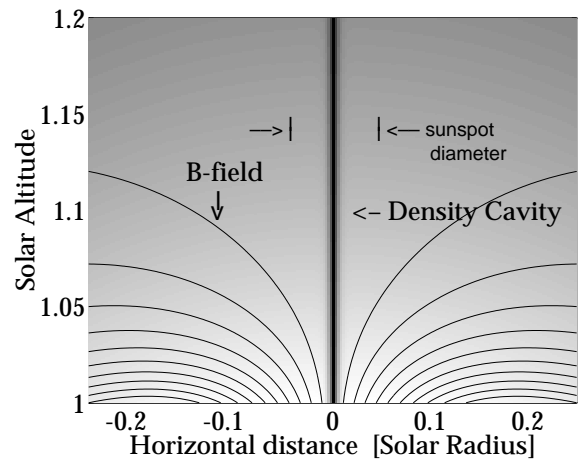

FIG. 2.—Two-dimensional representation of the model unipolar magnetic field lines, together with a gray-scale density plot, which includes a density cavity with footpoint at the center of the sunspot.

tude increases. The interior of the density duct is, therefore, modeled by the depleted density profile given by

$$n_e^I(r) = \frac{n_e^O(r)}{10^2 g(r) + 1} \ , \quad g(r) = 1 - \tanh \frac{r - 5\,R_\odot}{2\,R_\odot} \ , \quad (7)$$

where the superscript "I" is meant to denote the "interior."

To complete the modeling of the electron density, we must construct the entire three-dimensional density profile. We want the density duct to be aligned with the radial magnetic field lines emanating from the center of the sunspot (this is just for the sake of convenience—the footpoint of the duct can be located anywhere within the sunspot, and there can be multiple ducts) but with a much smaller radius at the base. We also model the density duct to stretch out radially with no variation along the angular direction. The following three-dimensional model is adopted for the present purpose:

$$n_e(r, \theta_P) = n_e^O(r) + \frac{n_e^O(r) - n_e^I(r)}{2 \tanh (a/\delta)}$$
$$\times \left(\tanh \frac{x - a}{\delta} - \tanh \frac{x + a}{\delta} \right) ,$$
$$x = r \sin \theta_P \qquad (8)$$

where a represents the characteristic width of the duct, and δ denotes the smoothness associated with the density duct wall. For specific choices, we take $a = 10^3$ km, which corresponds to $a/R_\odot = 1.43 \times 10^3$. Considering that the normalized sunspot radius is given by $b/R_\odot = 0.0452$, the present choice of duct radius represents a much smaller dimension when compared to the sunspot size ($a/b \approx 0.032$). For the smoothness parameter, δ, we simply choose $\delta/R_\odot = 0.005$. The specific choice of δ is not critical. The gray-scale density plot shown as a backdrop in Figure 2 has been generated according to the model described in equation (8).

The local plasma frequency is given by

$$f_{\rm pe}(r, \theta_P) = 8.98 \times 10^{-3} n_e^{1/2}(r, \theta_P) \ {\rm MHz} \ . \qquad (9)$$

The angular plasma frequency is alternatively given by $\omega_{\rm pe}(r, \theta_P) = 2\pi f_{\rm pe}(r, \theta_P) = 5.64 \times 10^4 n_e^{1/2}(r, \theta_P)$ rad s^{-1}. Plotted in Figure 3a is the ratio $f_{\rm pe}(r, \theta_P)/f_{\rm ce}(r, \theta_P)$ as a function of normalized solar altitude and normalized horizontal distance. Figure 3b plots the same ratio computed inside and outside of the density duct. Note from both Figures 3a and 3b that the ratio $f_{\rm pe}/f_{\rm ce}$ remains small inside the duct, but rapidly rises as one approaches the duct wall. The ratio $f_{\rm pe}/f_{\rm ce}$ gradually rises as the altitude increases. Plasma characterized by the condition $f_{\rm pe}/f_{\rm ce} < 1$ is favorable to the excitation of the X and O electromagnetic modes with frequencies in the vicinities of the first few electron gyroharmonics by the cyclotron maser instability mechanism, provided there exists a free energy source (i.e., nonthermal energetic electrons), which is discussed next.

2.3. Model of Energetic Electrons

In what follows we use the normalized momentum, $\boldsymbol{u} = \boldsymbol{p}/m_e c$. In the cylindrical coordinate system we may write $\boldsymbol{u} = (u_\perp, u_\parallel)$, where $\perp$ and $\parallel$ denote directions perpendicular and parallel with respect to the local magnetic field, respectively. In a spherical coordinate system, we may alternatively write $\boldsymbol{u} = (u, \mu)$, where $u = (u_\perp^2 + u_\parallel^2)^{1/2}$ and $\mu = u_\parallel/u$. The total electron distribution function is considered to be a combination of a background (thermal) component and a tenuous energetic (nonthermal) electron beam component. The beam electrons are modeled to represent a quasi-monoenergetic distribution with a nonzero average pitch angle and possessing momentum dispersion in both energy and pitch-angle space.
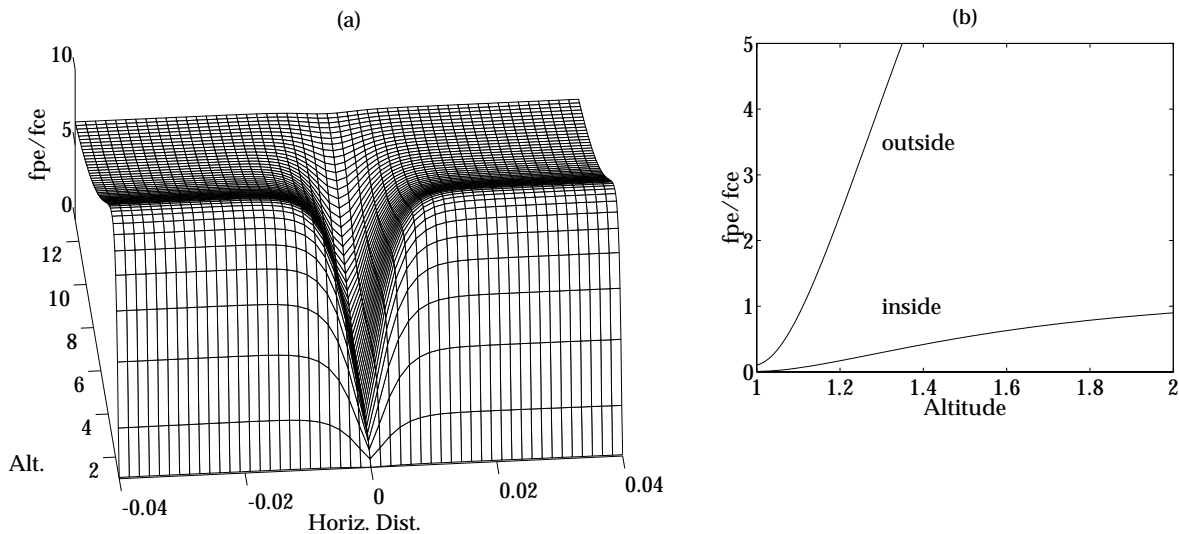

FIG. 3.—(a) Plot of the ratio of $f_{\rm pe}/f_{\rm ce}$ vs. solar altitude and a horizontal distance (both normalized to solar radius). The deep valley in the middle represents the density duct. The horizontal range roughly covers the entire sunspot. (b) Comparison of the same ratio when the horizontal coordinate is chosen at $x = 0$ (i.e., "inside" the density duct) vs. the asymptotic value ($x \gg 1$, designated as the "outside" value).

We choose the following form for the electron distribution:

$$F_e(u,\mu) = f_0(u) + \frac{n_b}{n_0}F_b(u,\mu), \quad F_0(u) = \frac{e^{-u^2/\alpha_0^2}}{(\sqrt{\pi}\alpha_0)^3} ,$$

$$F_b(u,\mu) = \frac{g(\mu)}{\pi^{3/2}\alpha^3 A_u A_\mu}\exp\left[-\frac{(u-u_0)^2}{\alpha^2}\right] ,$$

$$g(\mu) = \text{sech}^2\frac{\mu-\mu_0}{\Delta\mu} , \qquad (10)$$

where $n_b \ll n_0$ is assumed (i.e., the number density of non-thermal electrons is much lower than the background component). If the average speed associated with the electron beam is v_0, then the quantity, u_0, is related to v_0 by $u_0 = (v_0/c)(1 - v_0^2/c^2)^{-1/2}$. The quantities, α_0^2 and α^2, are the electron thermal energy normalized to mass energy corresponding to the background and energetic components, respectively. The quantity, μ_0, represents the cosine of the average pitch angle, and $\Delta\mu$ designates the spread in pitch angle. The normalization constants, A_u and A_μ, are given by

$$A_u = \left(1 + \frac{2u_0^2}{\alpha^2}\right)\left(1 + \text{erf}\,\frac{u_0}{\alpha}\right) + \frac{2}{\sqrt{\pi}}\frac{u_0}{\alpha}e^{-u_0^2/\alpha^2} ,$$

$$A_\mu = \frac{\Delta\mu}{2}\left(\tanh\frac{1-\mu_0}{\Delta\mu} + \tanh\frac{1+\mu_0}{\Delta\mu}\right) . \qquad (11)$$

In what follows, we impose some simplifying assumptions. In reality, as the beam electrons travel along the magnetic flux tube, the electron distribution should evolve in time (or in space, if viewed from the coordinate system moving with the average electron speed). However, to simplify the matter, we will consider that the phase-space distribution remains largely unchanged. This is, of course, a gross oversimplification of the actual situation. However, to discuss the actual beam evolution along the flux tube is very complicated as the evolution of the beam electron distribution will be affected not only by adiabatic phase-space volume conservation but also by a self-consistent wave-induced momentum space diffusion process. For the present purpose, we will simply adopt the assumption that energetic electrons possessing free energy are available within the radio source region. For specific choices of parameters, we adopt $\alpha = 0.05$, $u_0 = 0.5$, $\mu_0 = 0.8$, and $\Delta\mu = 0.5$. Figure 4 shows the plot of the model energetic electron distribution.

The number density associated with the beam electrons, n_b, is of interest. Note that in our model, the energetic electrons do not necessarily exist only within the density duct, since the physical mechanism that creates the density duct and the generation mechanism for energetic electrons may be unrelated to each other. To model the number density of the energetic electrons in a quantifiable manner is extremely difficult. To simplify the analysis, therefore, we will simply model the energetic electrons to have a number density that is directly proportional to the local electron density, but with a small scaling factor,

$$n_b(x,z) = \hat{n}n_e(x,r) , \qquad (12)$$

where $\hat{n}$ is the said scaling factor. We choose $\hat{n} = 0.001$ throughout the present analysis.
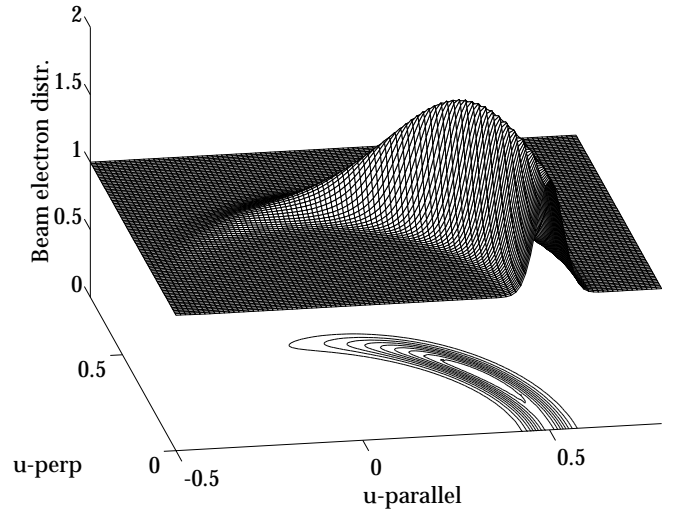

FIG. 4.—Model beam electron distribution, where $u_\parallel > 0$ is the upward direction.

2.4. Cyclotron Maser Instability

The presence of the energetic electrons together with low f_{pe}/f_{ce} inside the density duct imply that the direct emission of radiation can take place via a cyclotron maser instability mechanism. The temporal cyclotron growth/damping rate, which includes the cyclotron damping by the background electrons, is given by

$$\gamma_\sigma = \frac{\pi f_{pe}^2}{2 f}\frac{1}{(1+T_\sigma^2)R_\sigma}\sum_{s=1,2,3,\ldots}\int d^3\boldsymbol{u}(1-\mu^2)$$

$$\times \delta\left(\sqrt{1+u^2} - \frac{sf_{ce}}{f} - N_\sigma u\mu\cos\theta\right)$$

$$\times \left\{\frac{f}{f_{ce}}[K_\sigma\sin\theta + T_\sigma(\cos\theta - N_\sigma u\mu)]\frac{J_s(b_\sigma)}{b_\sigma} + J_s'(b_\sigma)\right\}^2$$

$$\times \left(u\frac{\partial}{\partial u} + (N_\sigma u\cos\theta - \mu)\frac{\partial}{\partial\mu}\right)F_e(u,\mu) ,$$

$$b_\sigma = \frac{f}{f_{ce}}N_\sigma\sin\theta u(1-\mu^2)^{1/2} . \qquad (13)$$

In the above, $\sigma = X, O$; N_σ represents the index of refraction for the X/O modes; $J_s(b)$ is the Bessel function of the first kind of order s; θ is the wave phase angle; and T_σ, R_σ, and K_σ are the so-called magnetoionic parameters. These are defined by

$$N_\sigma^2 = \epsilon_\sigma , \quad \epsilon_X = 1 - \frac{f_{pe}^2}{f(f+\tau f_{ce})} ,$$

$$\epsilon_O = 1 - \frac{\tau f_{pe}^2}{f(\tau f - f_{ce}\cos\theta)} ,$$

$$\tau = \left(s + \sqrt{\cos^2\theta + s^2}\right)\frac{f_{pe}^2 - f^2}{|f_{pe}^2 - f^2|} , \quad s = \frac{f f_{ce}\sin^2\theta}{2|f^2 - f_{pe}^2|} ,$$

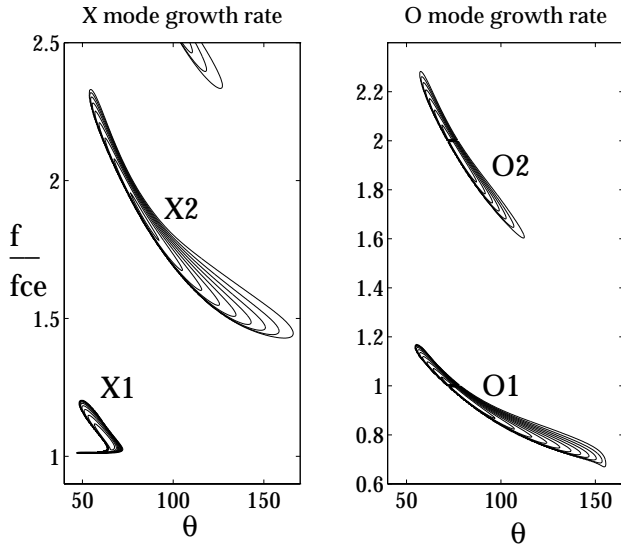$$R_X = 1 - \frac{\tau f_{pe}^2 f_{ce}(1+U)}{2f(f+\tau f_{ce})^2} ,$$

FIG. 5.—Temporal growth rates for *X*- and *O*-modes. *X*1, *X*2, *O*1, and *O*2, etc. represent *X*/*O*-modes excited at fundamental and (first) harmonic gyrofrequencies (f_{ce} and $2f_{ce}$), respectively. This figure corresponds to $f_{pe}/f_{ce} = 0.1$.
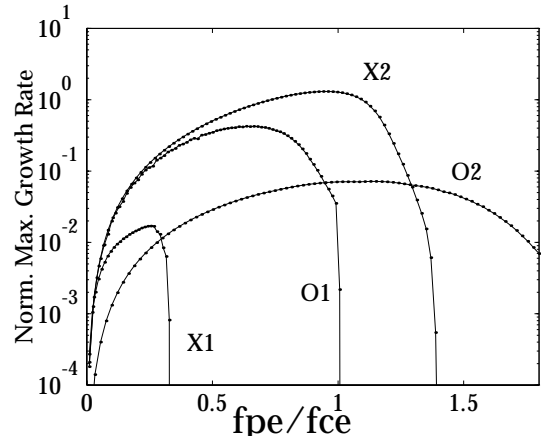

FIG. 6.—Plot of normalized maximum growth rate, $(n_0/n_b)(\gamma_{max}/f_{ce})$ as a function of f_{pe}/f_{ce}. This plot shows which modes will be locally excited when the parameter f_{pe}/f_{ce} varies continuously.

$$R_O = 1 + \frac{\tau f_{pe}^2 f_{ce} \cos^2 \theta (1 - U)}{2f(\tau f - f_{ce} \cos \theta)^2} ,$$

$$U = \frac{\tau^2 - \cos^2 \theta f^2 + f_{pe}^2}{\tau^2 + \cos^2 \theta f^2 - f_{pe}^2} ,$$

$$T_X = -\frac{\cos \theta}{\tau} , \quad T_O = \frac{\tau}{\cos \theta} ,$$

$$K_X = \frac{f_{pe}^2}{f^2 - f_{pe}^2} \frac{f_{ce} \sin \theta}{f + \tau f_{ce}} , \quad K_O = \frac{f_{pe}^2}{f^2 - f_{pe}^2} \frac{\tau f_{ce} \sin \theta}{\tau f - f_{ce} \cos^2 \theta} .$$

$$(14)$$

With the model distribution from equation (12), we have numerically calculated the growth rate (eq. [13]) for $f_{pe}/f_{ce} = 0.1$ and for an arbitrary value of the density ratio, $n_b/n_0 = 10^{-3}$. Other parameters are the same as considered in Figure 4. The result is plotted in Figure 5. The meaning of the mode designations such as *X*1, *X*2, *O*1, *O*2, etc. is obvious; *X*1 represents the *X*-mode with an excitation frequency in the vicinity of f_{ce}, *X*2 means the *X*-mode with a frequency near $2f_{ce}$, and so on.

Among the physical parameters that affect the temporal growth of the cyclotron modes, the ratio f_{pe}/f_{ce} is the most important factor that determines which mode should be locally excited, damped, or remain marginally stable. This property of the cyclotron maser instability is best described when the maximum temporal growth rate—determined over the entire two-dimensional parameter space of frequency versus angle space, (f,θ), for a given value of f_{pe}/f_{ce}—is plotted against f_{pe}/f_{ce}. Such a plot is shown in Figure 6. The key features are that for low f_{pe}/f_{ce} (say less than 0.3 or so), all three modes, i.e., *X*1, *X*2, and *O*1 are excited, while for f_{pe}/f_{ce} greater than ~ 0.3 but less than unity, only *X*2- and *O*1-modes are predicted to grow. For f_{pe}/f_{ce} between 1 and ~ 1.5 or so, only the *X*2-mode should

be excited. The *O*2-mode growth rate is, by and large, unimportant when compared with other modes.

On the basis of this finding, which was obtained with the local growth rate computation, one might be tempted to conclude that in the case of pair emission, when the radiation source (electron beam) is in the lower corona where f_{pe}/f_{ce} is very small, the emitted fundamental radiation should be in the mixed polarization (*X*1 and *O*1), while the harmonic component should be an *X*-mode (*X*2). One might go on to conclude that as the source moves to higher altitudes, then at some point, the *X*-mode component associated with the fundamental emission should gradually disappear, so that it would be dominated by the *O*-mode. Such a conclusion is, of course, at variance with some of the reported observations. However, as we will discuss in the next subsection, the local growth rate property is only part of the story. To definitively test the present scenario, one must compute the convective amplification of the electromagnetic rays as they move up the density duct, while undergoing multiple reflections off the density cavity wall.

We will demonstrate that the *O*-mode rays do not have significant saturation amplitudes while *X*1- and *X*2-modes both reach comparable intensities as a result of spatial amplification and saturation. This finding implies that the pair emission under the present scenario should be polarized in the same sense of *X*-mode polarization for both the fundamental and harmonic components. Let us discuss this in detail next.

2.5. *Convective Amplification of Rays*

The time rate of change in the electromagnetic ray intensity along the ray path can be determined by the wave kinetic equation,

$$dI_\sigma/dt = S_\sigma + 2\gamma_\sigma I_\sigma , \quad (15)$$

which is applicable along the ray paths, and where $I_\sigma(f, \theta, t)$ is the ray energy per unit frequency and phase angle. The quantity S_σ is the spontaneously emitted spectral

power,

$$S_\sigma = \pi \frac{f_{pe}^2}{f^2} \frac{m_e c^2}{(1 + T_\sigma^2) R_\sigma} \sum_{s=1,2,3,\ldots} \int d^3 \boldsymbol{u} (1 - \mu^2)$$

$$\times \delta \left(\sqrt{1 + u^2} - \frac{s f_{ce}}{f} - n_\sigma u \mu \cos\theta \right)$$

$$\times \left\{ \frac{f}{f_{ce}} [K_\sigma \sin\theta + T_\sigma (\cos\theta - N_\sigma u \mu)] \frac{J_s(b_\sigma)}{b_\sigma} + J_s'(b_\sigma) \right\}^2$$

$$\times u^2 F_e(u, \mu) . \tag{16}$$

One can easily show that if there were no energetic electrons so that all the electrons are in thermal equilibrium, then the relation

$$\gamma_\sigma = \frac{-f S_\sigma}{(m_e c^2 \alpha_0^2)}$$

between S_σ and γ_σ exists, and the wave intensity would not change in time, as a result of the balance between the spontaneous emission and induced absorption. This implies that the equilibrium electromagnetic intensity spectrum $(dI_\sigma^{equil}/dt = 0)$ can be determined as

$$I_\sigma^{equil} = \frac{T_e}{f} .$$

When the beam electrons are present, the left-hand side of equation (15) is finite $(dI_\sigma/dt \neq 0)$ so that the ray intensity can either amplify or damp along the ray paths. It turns out that the spontaneous emission term plays a key role in the wave amplification process. The numerical results will show that despite the linear growth rate property, the O-mode rays generally do not reach any appreciable amplitude, while for the frequency range of interest to solar radio physics, both $X1$- and $X2$-modes undergo significant amplifications. This can be only understood from the disparity associated with the terms S_X and S_O in equation (15). A preliminary discussion of this point was already put forth in the discussion by Wu et al. (2002), where they showed that spontaneously generated O-mode wave power is much weaker than that of the X-mode. To put it simply, the comparative magnitudes of the temporal growth rate, γ_X and γ_O, are insufficient in solving for the intensities, I_X and I_O, but we must also consider S_X and S_O. The present analysis includes both.

We reiterate that the wave kinetic equation (15) must be solved along the ray paths. The ray trajectory can be determined from the ray tracing equation, which is given by

$$\frac{dx}{dt} = \frac{c N_\sigma}{R_\sigma} \sin\theta (1 - P_\sigma) , \qquad \frac{dy}{dt} = 0 ,$$

$$\frac{dz}{dt} = \frac{c N_\sigma}{R_\sigma} \cos\theta (1 + P_\sigma \tan^2\theta) ,$$

$$\frac{d\theta}{dt} = \frac{c}{2 N_\sigma R_\sigma} \left[S_\sigma \sin\theta \left(\cos\theta_P \frac{1}{B} \frac{\partial B}{\partial r} - \frac{\sin\theta_P}{r} \frac{1}{B} \frac{\partial B}{\partial \theta_P} \right) \right.$$

$$- Q_\sigma (\cos\phi \cos\theta \sin\theta_P - \sin\theta \cos\theta_P) \frac{1}{n_e} \frac{\partial n_e}{\partial r}$$

$$\left. - \frac{Q_\sigma}{r} (\cos\phi \cos\theta \cos\theta_P + \sin\theta \sin\theta_P) \frac{1}{n_e} \frac{\partial n_e}{\partial \theta_P} \right] , \tag{17}$$

where

$$x = r \cos\phi \sin\theta_P , \qquad y = r \sin\phi \sin\theta_P ,$$

$$z = r \cos\theta_P ,$$

$$P_X = -\frac{\tau f_{pe}^2 f_{ce} (1 - V)}{2 N_X^2 f (f + \tau f_{ce})^2} , \qquad P_O = \frac{\tau f_{pe}^2 f_{ce} \cos^2\theta (1 + V)}{2 N_O^2 f (\tau f - f_{ce} \cos^2\theta)^2} ,$$

$$Q_X = \frac{f_{pe}^2}{f (f + \tau f_{ce})} \left(1 - Y \frac{\tau f_{ce}}{f + \tau f_{ce}} \right) ,$$

$$Q_O = \frac{\tau f_{pe}^2}{f (\tau f - f_{ce} \cos^2\theta)} \left(1 - Y \frac{f_{ce} \cos^2\theta}{\tau f - f_{ce} \cos^2\theta} \right) ,$$

$$S_X = -\frac{2\tau^2}{\tau^2 + \cos^2\theta} \frac{\tau f_{pe}^2 f_{ce}}{f (f + \tau f_{ce})^2} ,$$

$$S_O = \frac{2 \cos^2\theta}{\tau^2 + \cos^2\theta} \frac{\tau f_{pe}^2 f_{ce} \cos^2\theta}{f (\tau f - f_{ce} \cos^2\theta)^2} ,$$

$$V = \frac{f f_{ce} (1 + \cos^2\theta)}{2 |f^2 - f_{pe}^2| \sqrt{s^2 + \cos^2\theta}} , \qquad Y = \frac{\tau^2 - \cos^2\theta}{\tau^2 + \cos^2\theta} \frac{f_{pe}^2}{f^2 - f_{pe}^2} . \tag{18}$$

Some examples of ray paths are shown in Figure 7. The rays shown below are all launched at $x = 0$ and at solar altitude $z = 1.1\ R_\odot$. The initial launch condition for these rays, i.e., the phase angle, θ, and the frequency, f, are not necessarily chosen according to the local maximum wave growth condition. These are chosen somewhat arbitrarily. The purpose of these rays is only to demonstrate the actual ray paths inside the duct. In the study of ray intensity calculation along the ray paths, to be presented subsequently, we will rigorously determine the initial phase angle and frequency on the basis of the local temporal growth condition. At any rate, for the moment, to simplify the discussion, let us choose the initial phase angles to be all set equal to $\theta = 90°$. For the X-mode, we launch two rays, one with frequency at 1.2 times the local electron gyrofrequency, $f = 1.2 f_{ce}$ (again, this is somewhat arbitrary), which represents an $X1$-mode, and the second ray with frequency $f = 1.9 f_{ce}$, which qualitatively represent $X2$. For the O-mode rays, we choose $f = 1.1 f_{ce}$ for the $O1$-ray, and $f = 1.9 f_{ce}$ for the $O2$-mode. As the figure shows, all the rays propagate up the field lines while undergoing multiple reflections off the density cavity wall. Observe that the harmonic modes ($X2$ and $O2$), owing to their higher frequencies, penetrate deeper into the density duct wall before they reflect.

Let us continue with the similar ray tracing calculation, but we now compute the ray intensities along the ray paths as well. For this purpose, as noted earlier, we need to proceed carefully and choose the initial conditions (θ and f) so that the rays with the optimal local growth conditions can be selected. We proceed with the following scheme: First, we choose the launch height of the initial ray (the horizontal location is the same for all rays, i.e., at the center of the duct, $x = 0$). For a given height, $z = R \cos\theta_P$, the local plasma frequency, $f_{pe}(x = 0, z)$, and the gyrofrequency, $f_{ce}(x = 0, z)$, as well as their ratio, f_{pe}/f_{ce}, are automatically known from the model density and magnetic field. We then compute the frequency and phase angle, (f, θ), corresponding to the most unstable mode, by carrying out a local insta-
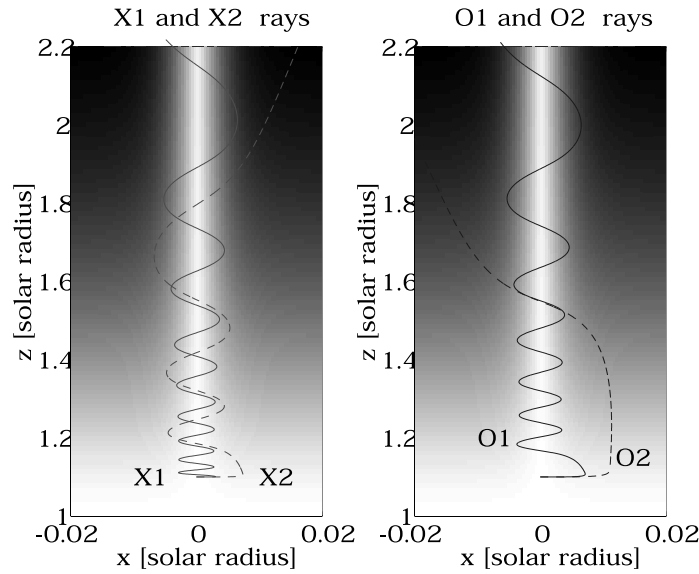
Fig. 7.—Sample ray trajectories. The solid lines correspond to rays with frequencies close to the fundamental (f_{ce}) electron gyrofrequencies, while the dashed lines represent rays with frequencies close to $2f_{ce}$. The gray-scale background indicates the electron density; the darker the area, the higher the density.

bility analysis over two-dimensional parameter space, (f, θ), and by choosing the maximum growth rate by surveying the entire two-dimensional f-θ space. This computation is done separately for the $X1$-, $O1$-, and $X2$-modes. The distinction between the $X1$- and $X2$-modes can be made by judiciously limiting the frequency ranges to be surveyed for the most unstable mode. The $X3$ and higher harmonic modes as well as $O2$ and higher modes are all ignored. We repeat a similar procedure as we move up to sources at higher altitudes.

The result of such a ray trajectory computation is shown in Figure 8. The source heights were chosen to be located at $z/R_\odot = 1.1, 1.11, 1.12, \ldots, 1.19, 1.2$, and 1.21. The altitudinal range of the sources are indicated in the figure. As mentioned, the choice of frequency and initial phase angle for

each ray was made in accordance with the temporal growth condition so that each ray corresponds to the fastest growing mode at the source location. As the rays move to different locations, however, the local physical condition changes spontaneously such that the initially most unstable mode may no longer correspond to the most unstable mode in the new location. This is owing to the detuning effect of the cyclotron resonance condition. The local growth rate may even turn negative (i.e., cyclotron damping or, equivalently, cyclotron absorption), which is why the local linear growth rate theory (Fig. 6) is not sufficient to determine the actual wave amplitudes. It should be noted that if the spontaneous emission term in equation (15) were not present, then the waves that are growing initially would all eventually damp away and be reduced to zero amplitudes ($I_\sigma \to 0$) since, eventually, the rays would all be out of resonance with the local cyclotron frequency. However, since the energetic electrons possess enough free energy, it turns out that the spontaneously emitted nonthermal cyclotron radiation is sufficient to overcome the damping effect to make the right-hand side of equation (15) positive for the rays under consideration.

As already mentioned, we have also simultaneously solved the wave kinetic equation (15) while computing the ray paths, so that the change in the ray intensity along the ray path can be calculated automatically. The result of such a computation is shown in Figure 9, in which ray intensities corresponding to the same rays as shown in Figure 8 are plotted versus time. To indicate the fact that the rays launched at lower altitudes possess higher frequencies, we have shifted the vertical axis in proportion to the ray frequency, so that the resulting cumulative plot resembles the dynamic spectrum. Take for instance, the ray emanating from the source located at $z_0/R_\odot = 1.1$. The gyrofrequency at the source is given by 248.3 MHz. The fastest growing $X1$-mode is determined from the local growth rate calculation as having frequency $f = 256.6$ MHz. Likewise, the $X2$- and $O1$-modes possessing maximum growth rates are determined as being $f = 451.9$ MHz and $f = 222.4$ MHz, respec-
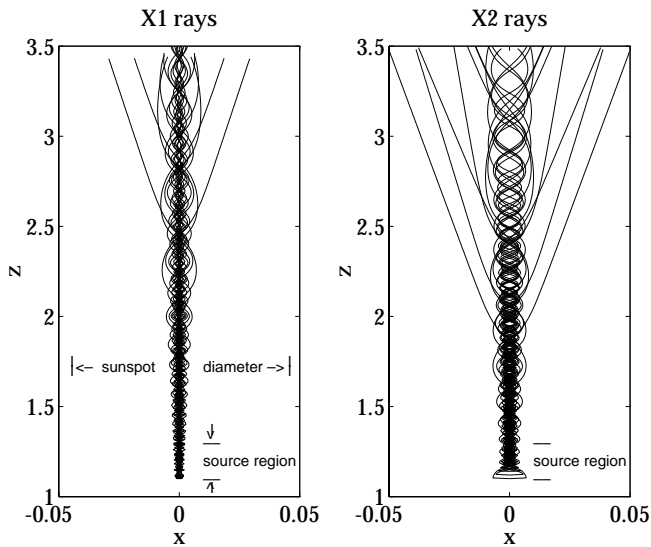

Fig. 8.—Ray trajectories with source heights located at $z/R_\odot = 1.1$, 1.11, 1.12, ..., 1.19, 1.2, and 1.21. The initial frequency and phase angle for each ray corresponds to the fastest growing mode.

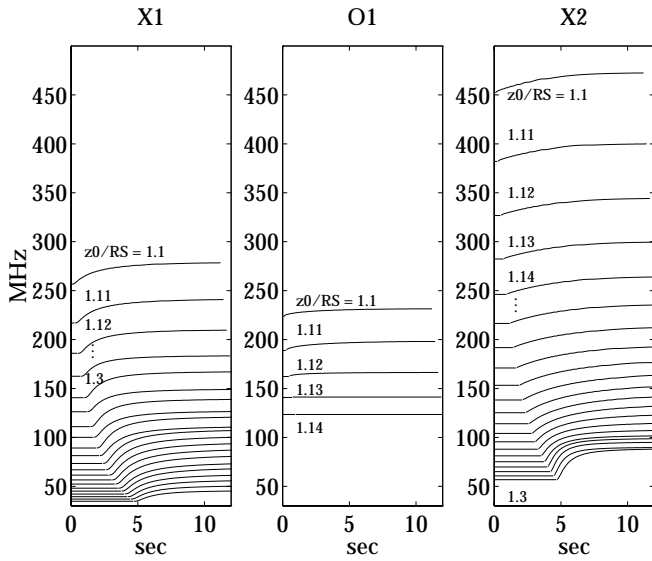FIG. 9.—Ray intensities corresponding to the rays whose paths are shown in Fig. 8. Note that $O1$-mode intensity is much lower than $X1$- and $X2$-mode intensities over the frequency range of practical importance, i.e., 30 MHz $\leq f \leq$ 200 MHz. Note also that $X1$- and $X2$-mode intensities possess comparable saturation magnitudes over the same frequency range. This shows that both the fundamental and harmonic components of the coronal type III bursts, according to the present emission mechanism, should be polarized in the sense of X-mode and that both components should have comparable magnitudes.
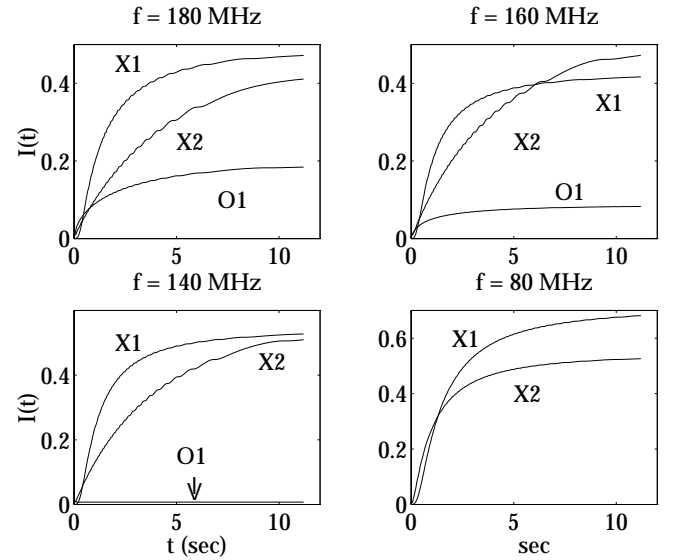

FIG. 10.—Plot of intensities $I_{X1}(t)$, $I_{X2}(t)$, and $I_{O1}(t)$ vs. time, computed at fixed frequencies. Four choices of frequency are adopted, namely, $f = 180$, 160, 140, and 80 MHz. Note that the asymptotic values of $I_{X1}(t)$ and $I_{X2}(t)$ are roughly comparable for all cases. In general, $I_{O1}(t)$ is much lower than $I_{X1}(t)$ and $I_{X2}(t)$. For 140 and 80 MHz frequencies, $I_{O1}(t)$ is altogether insignificant.

tively. Armed with this information, we have shifted the intensities $I_{X1}(t)$, $I_{O1}(t)$, and $I_{X2}(t)$ corresponding to $z_0/R_\odot = 1.1$ along the vertical axis by 256.6, 222.4, and 451.9, respectively. Moving on to the next source location, $z_0/R_\odot = 1.11$, we find that the $X1$-, $O1$-, and $X2$-modes possess frequencies of 217, 188.9, and 382.1 MHz. Correspondingly, we have shifted the intensities along the vertical axis by the same respective numbers.

We have further manipulated the result in another way to mimic the dynamic spectrum. That is, we have arbitrarily and successively delayed each plot along the time axis to represent the source motion. This was done in accordance with the recognition that sources at higher altitudes (and lower frequencies) should emit rays with a time delay equal to the time-of-flight effect associated with the average source motion. We have assumed that the source is moving up the field at a constant average speed of $0.1c$.

Note that the frequency range of interest to the actual solar radio astronomy is between $\sim$30 and $\sim$200 MHz. We have included higher frequency ranges only for the sake of discussion. The first important point to note is that the $O1$-mode amplification only occurs when the sources are at relatively low altitudes (i.e., a high-frequency regime that is not of practical interest) and that the convective amplification ceases to be effective in the actual frequency range of interest. Note also that, although the local linear growth rate plot in Figure 6 indicates that the $X1$-mode should possess a much lower growth rate than the $X2$-mode (if the amplification process is dictated by temporal growth), the two modes attain comparable amplitudes in the quasi-saturation stage.

To see this even more clearly, we have replotted some of the data already shown in Figure 9, in a new format. That is, in Figure 10 we have plotted the intensities $I_{X1}(t)$, $I_{X2}(t)$, and $I_{O1}(t)$ computed at fixed frequencies versus time, without

the artificial time delay. Four choices of frequency are adopted, namely, $f = 180$, 160, 140, and 80 MHz. Note that the asymptotic values of $I_{X1}(t)$ and $I_{X2}(t)$ are roughly comparable for all cases. In general, $I_{O1}(t)$ is much lower than $I_{X1}(t)$ and $I_{X2}(t)$. For 140 and 80 MHz frequencies, $I_{O1}(t)$ is altogether insignificant. This figure clearly shows that the $O1$-mode is generally insignificant and that both fundamental and harmonic components should be polarized in the sense of the X-mode having comparable intensities.

3. CONCLUSIONS

In this article, which complements the paper by Wu et al. (2002), a new scenario of the generation of type III radio emission, which involves radiation emission by cyclotron maser instability, is further explored by means of numerical computation of ray intensities. According to the discussion by Wu et al. (2002), which is limited to linear grow rate computation, the levels of the excited wave modes could not be estimated. As a result, a number of theoretical issues remained outstanding. Among them, local growth rate calculations show that $X1$-mode can have growth rate which is much higher (lower) than that of $X2$-mode if the amplification is dictated by spatial (temporal) growth, which is not consistent with observations. Another tentative conclusion that one may draw on the basis of local theory is that the $O1$-mode should be as important as the $X1$-mode, which is again not supported by observations.

To address these issues, one must compute the saturated wave intensities. For this purpose, we have formulated and solved the equations for ray trajectory and wave amplitude evolution under the model magnetic field and density duct. According to our numerical results, it is found that, for all practical purposes, the $O1$-mode amplitude is insignificant. Second, we found that both the $X1$- and $X2$-modes attain

comparable amplitudes in the saturation stage. The present findings imply that both the fundamental and harmonic components of the coronal type III pair emissions should be polarized in the sense of the *X*-mode and that both components should have comparable intensities, thus further strengthening the alternative scenario of coronal type III bursts by Wu et al. (2002). These findings could not be predicted on the basis of local linear theory.

Before we close, we reiterate that the present study is based on a highly simplified model of a solar magnetic flux tube and density duct (eqs. [4] and [8]). In principle, one could use a self-consistent magnetic and density model calculated on the basis of magnetohydrodynamic (MHD) simulations, instead of the present simplified model. For instance, numerical models of small-scale solar magnetic flux tubes have been carried out (Steiner et al. 1986, 1998). Although these works were motivated by structures in the photosphere and, as such, their simulations barely reach the chromosphere, much less the bottom of the corona, the gen-eral methodology can be applied to the simulation of the lower coronal magnetic field and density structures. Having obtained more realistic models, one could then incorporate the ray tracing/intensity calculation into these models and study features associated with type III bursts that cannot be studied with the present simple approach, such as self-absorption or striation. These are obviously beyond the scope of the present work, but should be pursued in the future.

REFERENCES

Dulk, G. A., & Suzuki, S. 1980, A&A, 88, 203
Newkirk, G., Jr. 1967, ARA&A, 5, 213
Steiner, O., Grossmann-Doerth, U., Knölker, M., & Schüssler, M. 1998, ApJ, 495, 468
Steiner, O., Pneuman, G. W., & Stenflo, J. O. 1986, A&A, 170, 126
Wu, C. S., Wang, C. B., Yoon, P. H., Zheng, H. N., & Wang, S. 2002, ApJ, in press
Zheleznyakov, V. V. 1970, Radio Emission of the Sun and Planets (New York: Pergamon)